

$\dot{R}_{out} T_d (T_{out}^{-1} - T_{in}^{-1})$, where \dot{R}_{out} is the outgoing long-wave radiation and T_{in} , T_{out} , and T_d are the mean temperature of atmospheric heat input, output, and dissipation, respectively. Observations of recent tropospheric warming [figures 2.26 and 2.27 in (32)] show that temperature trends are somewhat uniform in the vertical, which suggests that the difference $T_{out}^{-1} - T_{in}^{-1}$ might increase more slowly than either T_{in} or T_{out} . This slower increase may explain why $\delta \dot{Q}_{total}$ does not follow a surface Clausius-Clapeyron scaling and why one would expect moist processes to limit the work output in simulations with anthropogenic forcing. Simulations over a wider range of climates would help verify this hypothesis.

Our comparison of thermodynamic cycles in CESM and MERRA show many similarities; however, we find that CESM requires less power to maintain its hydrological cycle than the reanalysis, due to the smaller amplitude of its moistening inefficiencies. We suggest that this difference might be a consequence of the idealized nature of parameterized convection schemes, and it is likely that it might also influence the response of CESM to anthropogenic forcing. Typically, convection schemes artificially transport moisture along a moist adiabat without accounting for the work needed to lift this moisture, but in the real world, this work is necessary to sustain precipitation. Any increase in global precipitation therefore requires an increase in work output; otherwise, precipitation would have to become more efficient, for example, by reducing the frictional dissipation of falling hydrometeors (11, 12). This is one reason we should interpret the constraint in work output in CESM as a constraint on the large-scale motions and not on the unresolved subgrid-scale convective events.

Our work illustrates a major constraint on the large-scale global atmospheric engine: As the climate warms, the system may be unable to increase its total entropy production enough to offset the moistening inefficiencies associated with phase transitions. This suggests that in a future climate, the global atmospheric circulation might comprise highly energetic storms due to explosive latent heat release, but in such a case, the constraint on work output identified here will result in fewer numbers of such events. Earth's atmospheric circulation thus suffers from the "water in gas problem" observed in simulations of tropical convection (6), where its ability to produce work is constrained by the need to convert liquid water into water vapor and back again to tap its fuel.

REFERENCES AND NOTES

1. L. Barry, G. C. Craig, J. Thuburn, *Nature* **415**, 774–777 (2002).
2. M. H. P. Ambaum, *Thermal Physics of the Atmosphere* (Wiley, Hoboken, 2010), pp. 203–220.
3. O. R. Wulf, L. Davis Jr., *J. Meteorol.* **9**, 80–82 (1952).
4. J. P. Peixoto, A. H. Oort, M. De Almeida, A. Tomé, *J. Geophys. Res.* **96** (D6), 10981 (1991).
5. R. Goody, Q. J. R. Meteorol. Soc. **126**, 1953–1970 (2000).
6. O. Pauluis, I. M. Held, *J. Atmos. Sci.* **59**, 125–139 (2002).
7. D. M. Romps, *J. Atmos. Sci.* **65**, 3779–3799 (2008).
8. S. Pascale, J. Gregory, M. Ambaum, R. Tailleur, *Clim. Dyn.* **36**, 1189–1206 (2011).
9. O. Pauluis, I. M. Held, *J. Atmos. Sci.* **59**, 140–149 (2002).
10. O. Pauluis, *J. Atmos. Sci.* **68**, 91–102 (2011).
11. O. Pauluis, V. Balaji, I. M. Held, *J. Atmos. Sci.* **57**, 989–994 (2000).
12. O. Pauluis, J. Dias, *Science* **335**, 953–956 (2012).
13. S. Sherwood, R. Roca, T. Weckwerth, N. Andronova, *Rev. Geophys.* **48**, RG2001 (2010).
14. I. Held, B. Soden, *J. Clim.* **19**, 5686–5699 (2006).
15. R. Caballero, P. L. Langen, *Geophys. Res. Lett.* **32**, L02705 (2005).
16. P. O'Gorman, T. Schneider, *J. Clim.* **21**, 5797–5806 (2008).
17. T. Schneider, P. A. O'Gorman, X. Levine, *Rev. Geophys.* **48**, RG3001 (2010).
18. G. Vecchi, B. Soden, *J. Clim.* **20**, 4316–4340 (2007).
19. R. Feistel et al., *Ocean Science* **6**, 91–141 (2010).
20. Materials and methods are available as supplementary material on Science Online.
21. K. Emanuel, *Atmospheric Convection* (Oxford Univ. Press, MIT, Oxford, 1994).
22. D. R. Johnson, *International Geophysics*, D. A. Randall, Ed. (Academic Press, Waltham, 2001), pp. 659–720.
23. P. R. Gent et al., *J. Clim.* **24**, 4973–4991 (2011).
24. R. H. Moss et al., *Nature* **463**, 747–756 (2010).
25. M. M. Rienerer et al., *J. Clim.* **24**, 3624–3648 (2011).
26. J. D. Zika, M. H. England, W. P. Sijp, *J. Phys. Oceanogr.* **42**, 708–724 (2012).
27. K. Döös, J. Nilsson, J. Nylander, L. Brodeau, M. Ballarotta, *J. Phys. Oceanogr.* **42**, 1445–1460 (2012).
28. J. Kjellsson, K. Döös, F. B. Laliberté, J. D. Zika, *J. Atmos. Sci.* **71**, 916–928 (2014).
29. S. Groeskamp, J. D. Zika, T. J. McDougall, B. M. Sloyan, F. Laliberté, *J. Phys. Oceanogr.* **44**, 1735–1750 (2014).
30. O. M. Pauluis, A. A. Mrowiec, *J. Atmos. Sci.* **70**, 3673–3688 (2013).
31. V. Lucarini, K. Fraedrich, F. Ragone, *J. Atmos. Sci.* **68**, 2438–2458 (2011).
32. D. L. Hartmann et al., Climate Change 2013: The Physical Science Basis. Contribution of Working Group I to the Fifth Assessment Report of the Intergovernmental Panel on Climate Change, T. F. Stocker et al., Eds. (Cambridge Univ. Press, Cambridge and New York, NY, USA, 2013).

ACKNOWLEDGMENTS

We acknowledge the Global Modeling and Assimilation Office (GMAO) and the Goddard Earth Sciences Data and Information Services Center (GES DISC) for the dissemination of MERRA data. This work was supported by the G8 Research Initiative grant "ExArch: Climate analytics on distributed exascale data archives" made available through the Natural Sciences and Engineering Research Council (NSERC).

SUPPLEMENTARY MATERIALS

www.sciencemag.org/content/347/6221/540/suppl/DC1
Materials and Methods
Supplementary Text
Figs. S1 to S5
References (33–36)

9 June 2014; accepted 3 December 2014
10.1126/science.1257103

OPTICAL IMAGING

Expansion microscopy

Fei Chen,^{1,*} Paul W. Tillberg,^{2,*} Edward S. Boyden^{1,3,4,5,6†}

In optical microscopy, fine structural details are resolved by using refraction to magnify images of a specimen. We discovered that by synthesizing a swellable polymer network within a specimen, it can be physically expanded, resulting in physical magnification. By covalently anchoring specific labels located within the specimen directly to the polymer network, labels spaced closer than the optical diffraction limit can be isotropically separated and optically resolved, a process we call expansion microscopy (ExM). Thus, this process can be used to perform scalable superresolution microscopy with diffraction-limited microscopes. We demonstrate ExM with apparent ~70-nanometer lateral resolution in both cultured cells and brain tissue, performing three-color superresolution imaging of ~10⁷ cubic micrometers of the mouse hippocampus with a conventional confocal microscope.

Microscopy has facilitated the discovery of many biological insights by optically magnifying images of structures in fixed cells and tissues. We here report that physical magnification of the specimen itself is also possible.

We first set out to see whether a well-known property of polyelectrolyte gels—namely, that dialyzing them in water causes expansion of the polymer network into extended conformations (Fig. 1A) (1)—could be performed in a biological sample. We infused into chemically

fixed and permeabilized brain tissue (Fig. 1B) sodium acrylate, a monomer used to produce superabsorbent materials (2, 3), along with the comonomer acrylamide and the cross-linker N,N'-methylenebisacrylamide. After triggering free radical polymerization with ammonium persulfate (APS) initiator and tetramethylethylenediamine (TEMED) accelerator, we treated the tissue-polymer composite with protease to homogenize its mechanical characteristics. After proteolysis, dialysis in water resulted in a 4.5-fold linear expansion, without distortion at the level of gross anatomy (Fig. 1C). Digestion was uniform throughout the slice (fig. S1). Expanded specimens were transparent (fig. S2) because they consist largely of water. Thus, polyelectrolyte gel expansion is possible when the polymer is embedded throughout a biological sample.

We developed a fluorescent labeling strategy compatible with the proteolytic treatment and subsequent tissue expansion described above,

¹Department of Biological Engineering, Massachusetts Institute of Technology (MIT), Cambridge, MA, USA.

²Department of Electrical Engineering and Computer Science, MIT, Cambridge, MA, USA. ³Media Lab, MIT, Cambridge, MA, USA. ⁴McGovern Institute, MIT, Cambridge, MA, USA. ⁵Department of Brain and Cognitive Sciences, MIT, Cambridge, MA, USA. ⁶Center for Neurobiological Engineering, MIT, Cambridge, MA, USA.

*These authors contributed equally to this work. †Corresponding author. E-mail: esb@mit.edu

to see whether fluorescence nanoscopy would be possible. We designed a custom fluorescent label (Fig. 1D) that can be incorporated directly into the polymer network and thus survives the proteolytic digestion of endogenous biomolecules. This label is trifunctional, comprising a methacryloyl group capable of participating in free radical polymerization, a chemical fluorophore for visualization, and an oligonucleotide that can hybridize to a complementary sequence attached to an affinity tag (such as a secondary antibody) (Fig. 1, E and F). Thus, the fluorescent tag is targeted to a biomolecule of interest yet remains anchored covalently with high yield (table S1) to the polymer network. The entire process of labeling, gelation, digestion, expansion, and imaging we call expansion microscopy (ExM).

We performed fluorescence imaging using ExM, examining microtubules in fixed human embryonic kidney (HEK) 293 cells labeled with the trifunctional label and imaged with confocal laser scanning microscopy pre- versus post-ExM processing. The post-ExM image (Fig. 2B) was registered to the pre-ExM image (Fig. 2A) via a similarity transformation, resulting in visually indistinguishable images. To quantify the isotropy of ExM, we calculated the deformation vector field between the images via a nonrigid registration process (fig. S3). From this vector field, we quantified the root-mean-square (RMS) error of feature measurements post-ExM. The

errors in length were small (<1% of distance, for errors larger than the imaging system point spread function size; $n = 4$ samples) (Fig. 2C). Throughout the paper, all distances measured in the post-expansion specimen are reported divided by the expansion factor (supplementary materials, materials and methods).

We next compared pre-ExM conventional superresolution images to post-ExM confocal images. We labeled features traditionally used to characterize the performance of superresolution microscopes, including microtubules (4, 5) and clathrin coated pits (6), and imaged them with a superresolution structured illumination microscope (SR-SIM) pre-ExM, and a spinning disk confocal post-ExM. Qualitatively (Fig. 2, D and E), the images were similar, and quantitatively (Fig. 2I), measurement errors were again on the order of 1% and well within the point spread function size of the SR-SIM microscope ($n = 4$ samples). Microtubule networks were more sharply resolved in ExM (Fig. 2G) than with SR-SIM (Fig. 2F). ExM resolved individual microtubules that could not be distinguished with SR-SIM (Fig. 2H). Microtubules imaged with ExM presented a full-width at half-maximum (FWHM) (Fig. 2J) of 83.8 ± 5.68 nm (mean \pm SD, $n = 24$ microtubules from 3 samples). This FWHM reflects the effective resolution of ExM convolved by the width of the labeled microtubule. To estimate the effective resolution of ExM, we deconvolved [as in (7)] our observed microtubule

FWHM by the known immunostained microtubule width [55 nm (6)], conservatively ignoring the width of the trifunctional label, and obtained an effective resolution for ExM of ~60 nm. This conservative estimate is comparable with the diffraction-limited confocal resolution [~ 250 -nm lateral resolution (8)] divided by the expansion factor (~4.5).

Clathrin-coated pits were also well resolved (Fig. 2, K and L). ExM resolved the central nulls of the pits better than SR-SIM (Fig. 2, M and N). Clathrin-coated pit radii measured via ExM and SR-SIM were highly correlated, with a slope of 1.001 (total least squares regression, confidence interval 0.013 with $P < 0.05$, $n = 50$ pits from three samples) (Fig. 2O). Forty-nine of the 50 points lay within a half-pixel distance of the unity slope line, suggesting that variation in the ExM versus SR-SIM comparison was within the digitization error of the measurement.

We next applied ExM to fixed brain tissue. Slices of brain from Thy1-YFP-H mice expressing cytosolic yellow fluorescent protein (YFP) under the Thy1 promoter in a subset of neurons (9) were stained with a trifunctional label bearing Alexa 488, using primary antibodies to green fluorescent protein (GFP) (which also bind YFP). Slices expanded fourfold, similar to the expansion factor in cultured cells. We compared pre- versus post-ExM images taken on an epifluorescence microscope. As with cultured cells, the post-ExM image (Fig. 3B) was registered to the pre-ExM

Fig. 1. Expansion microscopy (ExM) concept. (A) Schematic of (i) collapsed polyelectrolyte network, showing crosslinker (dot) and polymer chain (line), and (ii) expanded network after H_2O dialysis. (B) Photograph of fixed mouse brain slice. (C) Photograph, post-ExM, of the sample (B) under side illumination. (D) Schematic of label that can be anchored to the gel at site of a biomolecule. (E) Schematic of microtubules (green) and polymer network (orange). (F) The label of (D), hybridized to the oligo-bearing secondary antibody top (top gray shape) bound via the primary (bottom gray shape) to microtubules (purple), is incorporated into the gel (orange lines) via the methacryloyl group (orange dot) and remains after proteolysis (dotted lines). Scale bars, (B) and (C) 5 mm. Schematics are not to scale.

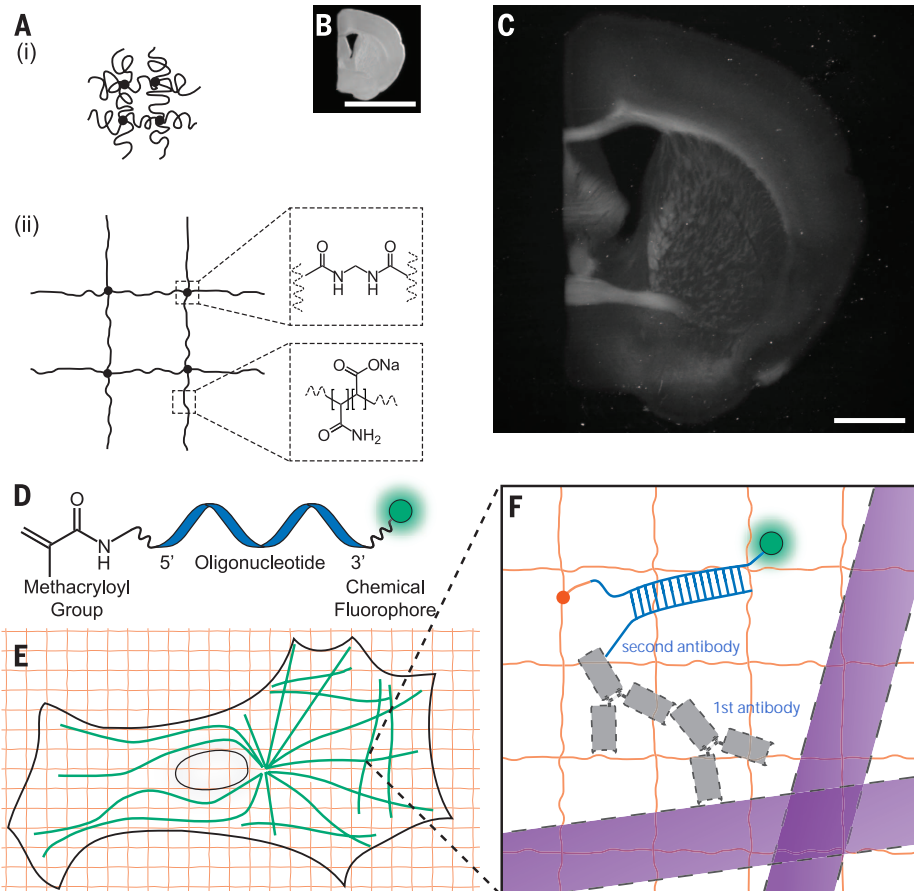


image (Fig. 3A) via a similarity transformation. The registered images closely matched, although some features moved in or out of the depth of field because of the axial expansion post-ExM. Quantitatively, post-ExM measurement errors (Fig. 3C, $n = 4$ cortical slices) were 2 to 4%.

We synthesized trifunctional labels with different colors and oligonucleotides (supplementary materials, materials and methods) to enable multicolor ExM. We obtained pre- (Fig. 3D) ver-

sus post-ExM (Fig. 3E) images of Thy1-YFP mouse cortex with ExM labels directed against YFP (Fig. 3E, green) and the pre- and postsynaptic scaffolding proteins Bassoon (Fig. 3E, blue) and Homer1 (Fig. 3E, red). In the pre-ExM image, Bassoon and Homer1 staining form overlapping spots at each synapse (Fig. 3F), whereas the post-ExM image (Fig. 3G) shows clearly distinguishable pre- and postsynaptic labeling. We quantified the distance between the Bassoon and

Homer1 scaffolds, as measured with ExM. We fit the distributions of Bassoon and Homer1 staining intensity, taken along the line perpendicular to the synaptic cleft (Fig. 3H, boxed region), to Gaussians (Fig. 3I). The Bassoon-Homer1 separation was 169 ± 32.6 nm (Fig. 3J, $n = 277$ synapses from four cortical slices), similar to a previous study using stochastic optical reconstruction microscopy (STORM) in the ventral cortex and olfactory bulb, which obtained ~ 150 nm

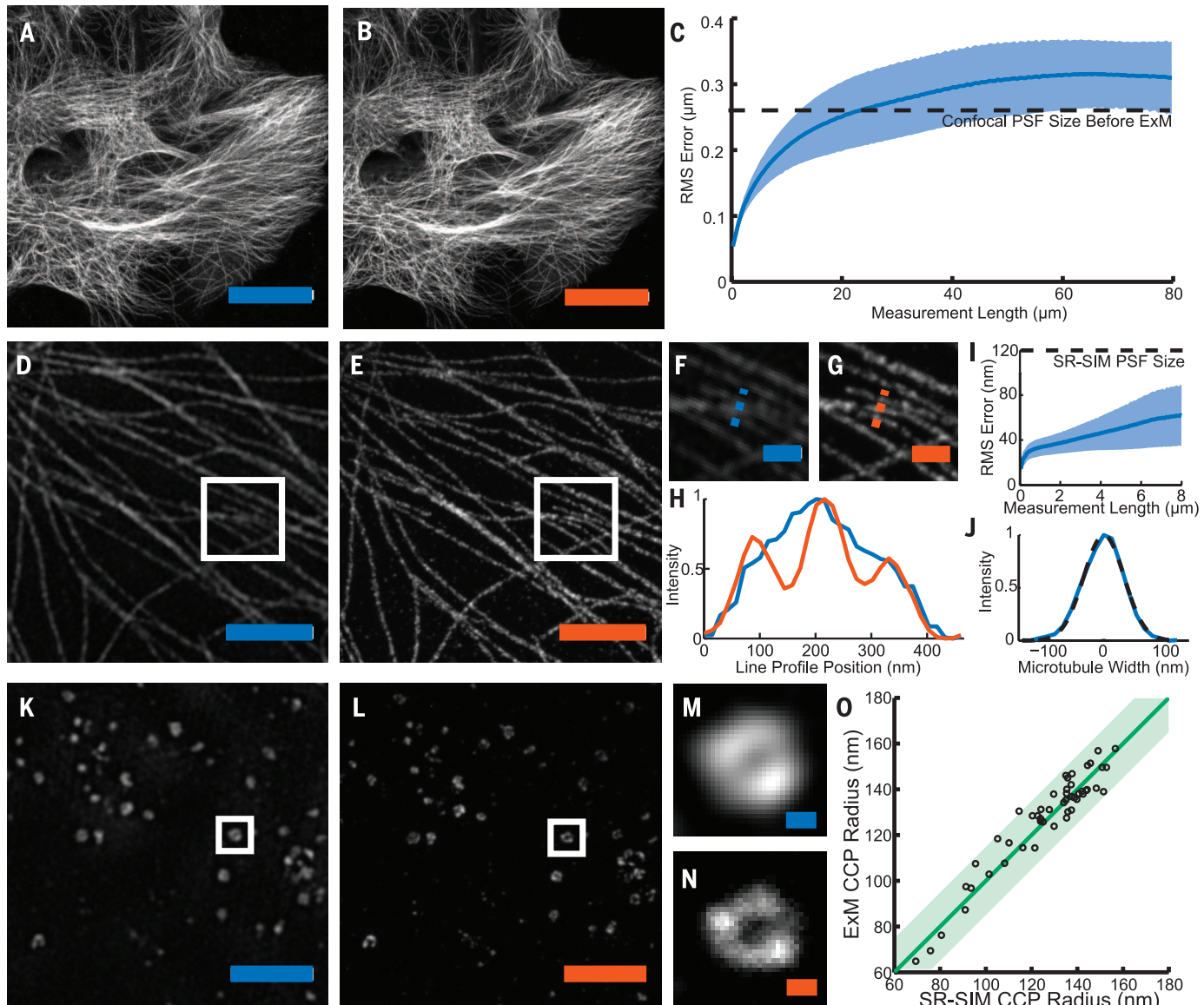


Fig. 2. Expansion microscopy physically magnifies, with nanoscale isotropy. We compared images acquired via conventional microscopy (blue scale bars) versus images acquired post-expansion (orange scale bars). (A) Confocal image of microtubules in HEK293 cells. (B) Post-expansion confocal image of sample (A). (C) RMS length measurement error of pre- versus post-ExM confocal images of cultured cells (blue line, mean; shaded area, standard deviation; $n = 4$ samples). (D) SR-SIM image of microtubules. (E) Post-expansion confocal image of the sample of (D). (F and G) Magnified views of boxed regions of (D) and (E), respectively. (H) Profiles of microtubule intensity taken along the blue and orange dotted lines in (F) and (G). (I) RMS length measurement error of ExM versus SR-SIM images (blue line,

mean; shaded area, standard deviation; $n = 4$ samples). (J) Transverse profile of a representative microtubule (blue line), with Gaussian fit (black dotted line). (K) SR-SIM image of clathrin-coated pits (CCPs) in HEK293 cells. (L) Post-expansion confocal image of the sample of (K). (M and N) Magnified views of a single CCP in the boxed regions of (K) and (L), respectively. (O) Scatterplot of radii of CCPs measured via ExM versus SR-SIM ($n = 50$ CCPs from 3 samples). Green line, $y = x$ line; shaded green region, half-pixel width of digitization error about the $y = x$ line. Scale bars for pre- versus post-ExM images, (A) 20 μm ; (B) 20 μm (physical size post-expansion, 81.6 μm); (D) 2 μm ; (E) 2 μm (9.1 μm); (F) 500 nm; (G) 500 nm (2.27 μm); (K) 2 μm ; (L) 2 μm (8.82 μm); (M) 100 nm; (N) 100 nm (441 nm).

separation (10). We also imaged other antibody targets of interest in biology (fig. S4).

To explore whether expanded samples, scanned on fast diffraction-limited microscopes, could support scalable superresolution imaging, we imaged a volume of the adult Thy1-YFP-H mouse brain spanning 500 by 180 by 100 μm (tissue slice thickness), with three labels (antibody to

GFP, green; antibody to Homer1, red; antibody to Bassoon, blue) (Fig. 4A). The diffraction limit of our confocal spinning disk microscope (with 40 \times , 1.15 NA, water immersion objective), divided by the expansion factor, yields an estimated effective resolution of ~70 nm laterally and ~200 nm axially. Shown in Fig. 4A is a three-dimensional (3D) rendered image of the data set (an ani-

mated rendering is provided in movie S1). Zooming into the raw data set, nanoscale features emerge (Fig. 4, B to D). We performed a volume rendering of the YFP-expressing neurons in a subset of CA1 stratum lacunosum moleculare (slm), revealing spine morphology (Fig. 4B and movie S2). Focusing on a dendrite in CA1 slm, we observed the postsynaptic protein Homer1

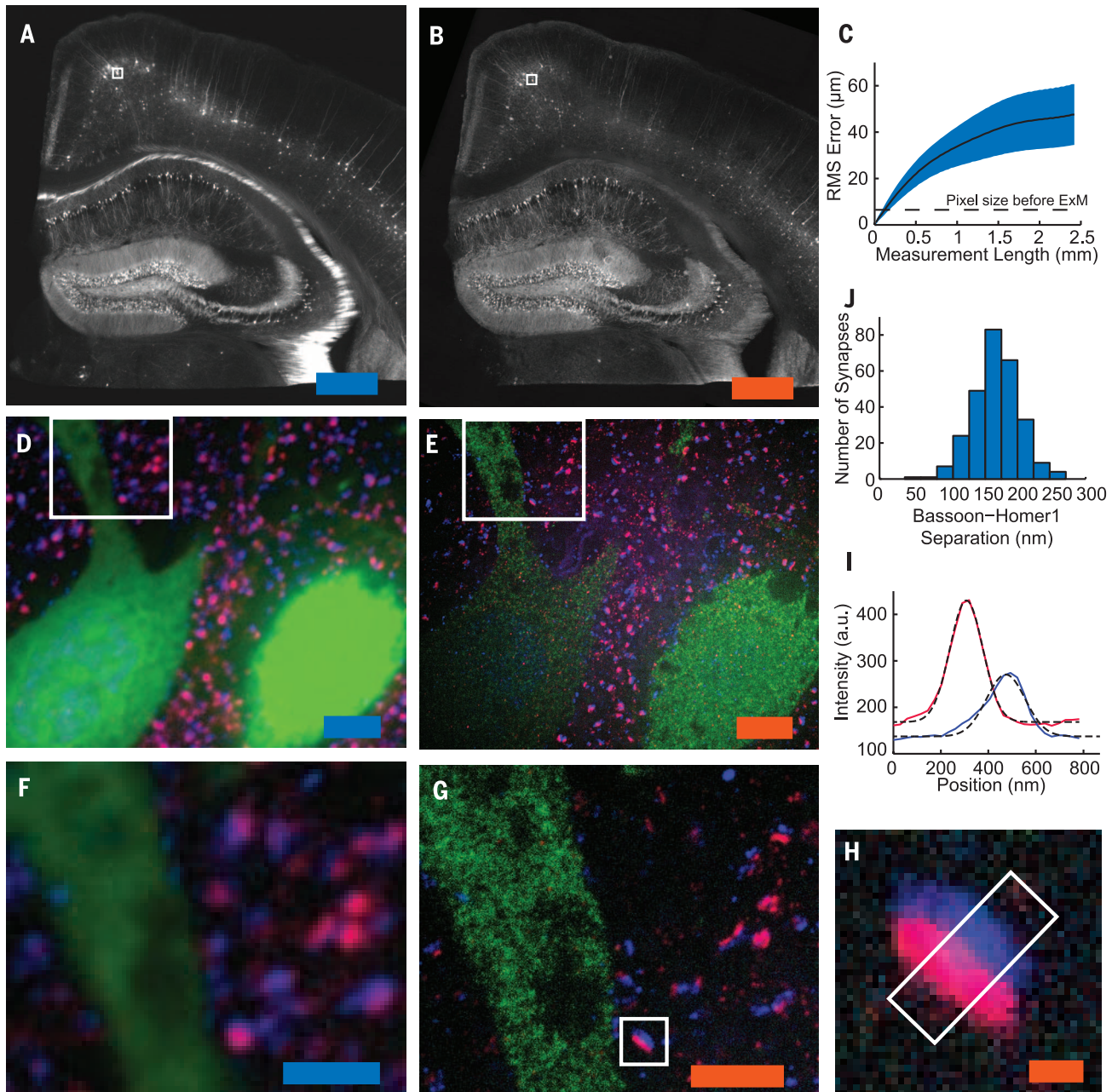


Fig. 3. ExM imaging of mammalian brain tissue. (A) Widefield fluorescence (white) image of Thy1-YFP mouse brain slice. (B) Post-expansion widefield image of sample (A). (C) RMS length measurement error for pre- versus post-ExM images of brain slices (blue line, mean; shaded area, SD; $n = 4$ samples). (D and E) Confocal fluorescence images of boxed regions in (A) and (B), respectively, stained with presynaptic (anti-Bassoon, blue) and postsynaptic (anti-Homer1, red) markers, in addition to antibody to GFP (green), pre- (D) versus post- (E) expansion. (F and G) Details of boxed

regions in (D) and (E), respectively. (H) Single representative synapse highlighted in (G). (I) Staining intensity for Bassoon (blue) and Homer1 (red) of the sample of (H) along white box long axis. Dotted black lines, Gaussian fits. a.u., arbitrary units. (J) Bassoon–Homer1 separation ($n = 277$) synapses from four cortical slices. Scale bars for pre- versus post-ExM images, (A) 500 μm ; (B) 500 μm (physical size post-expansion 2.01 mm); (D) 5 μm ; (E) 5 μm (20.1 μm); (F) 2.5 μm ; (G) 2.5 μm (10.0 μm); and (H) 250 nm (1.00 μm).

to be well localized to dendritic spine heads, with the presynaptic molecule Bassoon in apposition (Fig. 4C and movie S3). Examination of a mossy fiber bouton in the hilus of the dentate gyrus reveals invaginations into the bouton by spiny excrescences of the opposing dendrite, as observed previously via electron microscopy (Fig. 4D) (11). Thus, ExM enables multiscale imaging and visualization of nanoscale features, across length scales relevant to understanding neural circuits.

We report the discovery of a new modality of magnification, namely that fixed cells and tissues, appropriately labeled and processed, can be physically magnified, with isotropic nanoscale resolution (effective ~60-nm lateral resolution). Although acrylate esters have been used for

antigen-preserving embedding for electron microscopy (12, 13), ExM represents the first use of an embedded polyelectrolyte gel, used here to expand the specimen. Superresolution imaging methods are slower than their diffraction-limited counterparts because they must resolve more voxels per unit volume. ExM achieves this by expanding the voxels physically. ExM achieves the same voxel throughputs as a diffraction-limited microscope, but at the voxel sizes of a superresolution microscope. Ongoing technology trends for faster diffraction-limited microscopy (14) will continue to boost ExM speed.

The physical magnification of ExM enables superresolution imaging with several fundamental new properties. The axial effective resolution is improved by the same factor as the

lateral effective resolution. ExM can achieve superresolution with standard fluorophores, and on a diffraction-limited microscope. Superresolution imaging is often performed within ~10 μm of the sample surface because of low signal-to-noise, scattering, and refractive index mismatch. We were able to perform three-color superresolution imaging of a large volume of brain tissue over an axial extent of 100 μm with a spinning disk confocal microscope. Because the ExM-processed sample is almost entirely water, eliminating scattering, ExM may empower fast methods such as light-sheet microscopy (15) to become superresolution methods. ExM potentially enables labels to be situated within a well-defined, *in vitro*-like environment, facilitating *in situ* analysis (16). Because the

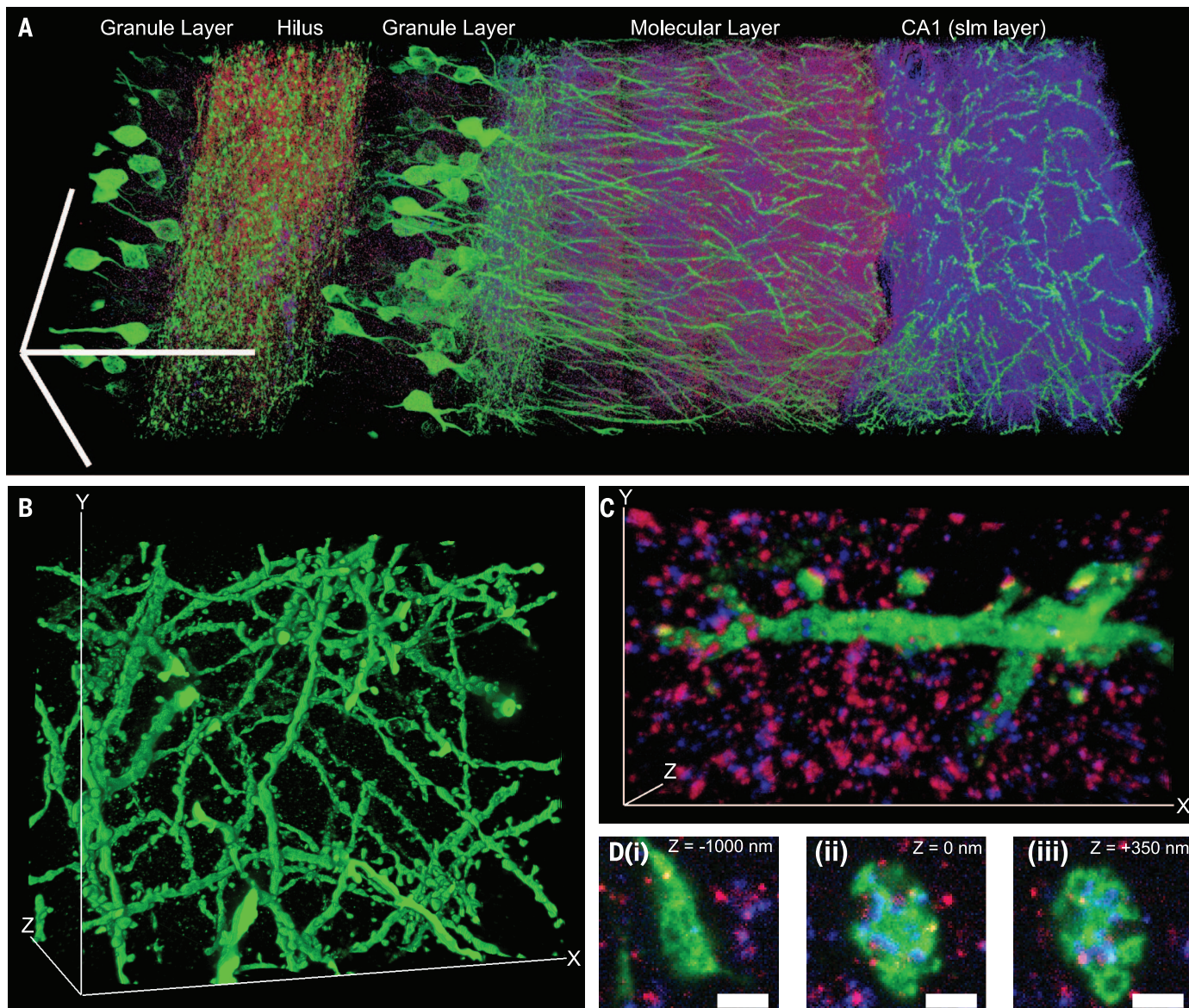


Fig. 4. Scalable 3D superresolution microscopy of mouse brain tissue. (A) Volume rendering of a portion of hippocampus showing neurons (expressing YFP, shown in green) and synapses [marked with anti-Bassoon (blue) and antibody to Homer1 (red)]. (B) Volume rendering of dendrites in CA1 slm. (C) Volume rendering of dendritic branch in CA1 slm. (D) Mossy fiber bouton in hilus of the dentate gyrus. (i) to (iii), selected z-slices. Scale bars, (A) 100 μm in each dimension; (B) 52.7 μm (x); 42.5 μm (y); and 35.2 μm (z); (C) 13.5 μm (x); 7.3 μm (y); and 2.8 μm (z); (D), (i) to (iii) 1 μm .

sample is physically larger, any mechanical errors in post-expansion sectioning, or stage drift, are divided by the expansion factor.

The performance of ExM suggests that despite statistical fluctuations in polymer chain length at the molecular scale, at the nanoscale distances here examined these fluctuations average out, yielding isotropy. Estimates of mesh size for comparable gels suggest that the distance between nearest-neighbor polymer chains are in the ~1 to 2 nm range (17, 18). By tuning the material properties of the ExM polymer, such as the density of cross-links, yet higher effective resolutions may be possible.

REFERENCES AND NOTES

- T. Tanaka et al., *Phys. Rev. Lett.* **45**, 1636–1639 (1980).
- I. Ohmine, *J. Chem. Phys.* **77**, 5725 (1982).
- F. L. Buchholz, *Superabsorbent Polymers* **573**, 27–38 (1994).
- B. Huang, S. A. Jones, B. Brandenburg, X. Zhuang, *Nat. Methods* **5**, 1047–1052 (2008).
- E. H. Rego et al., *Proc. Natl. Acad. Sci. U.S.A.* **109**, E135–E143 (2012).
- M. Bates, B. Huang, G. T. Dempsey, X. Zhuang, *Science* **317**, 1749–1753 (2007).
- N. Olivier, D. Keller, P. Gönczy, S. Manley, *PLOS One* **8**, e63020 (2013).
- R. W. Cole, T. Jinadasa, C. M. Brown, *Nat. Protoc.* **6**, 1929–1941 (2011).
- G. Feng et al., *Neuron* **28**, 41–51 (2000).
- A. Dani, B. Huang, J. Bergan, C. Dulac, X. Zhuang, *Neuron* **68**, 843–856 (2010).
- A. Rollenhagen, J. H. R. Lübke, *Front. Synaptic Neurosci.* **2**, 2 (2010).
- G. R. Newman, B. Jasani, E. D. Williams, *Histochem. J.* **15**, 543–555 (1983).
- K. D. Micheva, S. J. Smith, *Neuron* **55**, 25–36 (2007).
- B.-C. Chen et al., *Science* **346**, 1257998 (2014).
- J. Huisken, J. Swoger, F. Del Bene, J. Wittbrodt, E. H. K. Stelzer, *Science* **305**, 1007–1009 (2004).
- J. H. Lee et al., *Science* **343**, 1360–1363 (2014).
- A. M. Hecht, R. Duplessix, E. Geissler, *Macromolecules* **18**, 2167–2173 (1985).
- D. Calvet, J. Y. Wong, S. Giasson, *Macromolecules* **37**, 7762–7771 (2004).

ACKNOWLEDGMENTS

E.S.B. was funded by NIH Director's Pioneer Award 1DP1NS087724 and NIH Director's Transformative Research Award 1R01MH03910-01, the New York Stem Cell Foundation-Robertson Investigator Award, the MIT Center for Brains, Minds, and Machines NSF CCF-1231216, Jeremy and Joyce Wertheimer, Google, NSF CAREER Award CBET 1053233, the MIT Synthetic Intelligence Project, the MIT Media Lab, the MIT McGovern Institute, and the MIT Neurotechnology Fund. F.C. was funded by an NSF Graduate Fellowship. P.W.T. was funded by a Fannie and John Hertz Graduate Fellowship. Confocal imaging was performed in the W. M. Keck Facility for Biological Imaging at the Whitehead Institute for Biomedical Research. DeltaVision OMX SR-SIM imaging was performed at the Koch Institute Swanson Biotechnology Center imaging core. We acknowledge W. Salmon and E. Vasile for assistance with confocal and SR-SIM imaging. We acknowledge N. Pak for assistance with perfusions. We also acknowledge, for helpful discussions, B. Chow, A. Marblestone, G. Church, P. So, S. Manalis, J.-B. Chang, J. Enriquez, I. Gupta, M. Kardar, and A. Wissner-Gross. The authors have applied for a patent on the technology, assigned to MIT (U.S. Provisional Application 61943035). The order of co-first author names was determined by a coin toss. The imaging and other data reported in the paper are hosted by MIT (<http://expansionmicroscopy.org/rawdataScience2014>).

SUPPLEMENTARY MATERIALS

www.sciencemag.org/content/347/6221/543/suppl/DC1
Materials and Methods

Figs. S1 to S5
Tables S1 to S4
References (19–28)
Movies S1 to S3

18 August 2014; accepted 26 November 2014
10.1126/science.1260088

MITOCHONDRIAL BIOLOGY

Replication-transcription switch in human mitochondria

Karen Agaronyan, Yaroslav I. Morozov, Michael Anikin, Dmitry Temiakov*

Coordinated replication and expression of the mitochondrial genome is critical for metabolically active cells during various stages of development. However, it is not known whether replication and transcription can occur simultaneously without interfering with each other and whether mitochondrial DNA copy number can be regulated by the transcription machinery. We found that interaction of human transcription elongation factor TEFM with mitochondrial RNA polymerase and nascent transcript prevents the generation of replication primers and increases transcription processivity and thereby serves as a molecular switch between replication and transcription, which appear to be mutually exclusive processes in mitochondria. TEFM may allow mitochondria to increase transcription rates and, as a consequence, respiration and adenosine triphosphate production without the need to replicate mitochondrial DNA, as has been observed during spermatogenesis and the early stages of embryogenesis.

The maternally inherited circular mitochondrial DNA (mtDNA) encodes subunits of complexes of the oxidative phosphorylation chain, as well as transfer RNAs (tRNAs) and ribosomal RNAs (1, 2). Transcription of human mtDNA is directed by two promoters, the LSP (light-strand promoter) and the HSP (heavy-strand promoter) located in opposing mtDNA strands, which results in two almost-genome-sized polycistronic transcripts that undergo extensive processing before polyadenylation and translation (3, 4). Note that transcription terminates prematurely about 120 base pairs (bp) downstream of LSP at a vertebrate-conserved G-rich region, called conserved sequence block II (CSBII), as a result of formation of a hybrid G-quadruplex between nascent RNA and the nontemplate strand of DNA (5–7). This termination event occurs near the origin of replication of the heavy strand (oriH) (8) and generates a replication primer. According to the asymmetric model (9), replication then proceeds through about two-thirds of the mtDNA, until the oriL sequence in the opposing strand becomes single stranded and forms a hairpin structure. The oriL hairpin is then recognized by mitochondrial RNA polymerase (mtRNAP), which primes replication of the light strand (10). Because replication of mtDNA coincides with transcription in time and space, collisions between transcription and replication machineries are inevitable and, similarly to bacterial and eukaryotic systems, likely have detrimental effects on mtDNA gene expression (11).

We analyzed the effects of a mitochondrial transcription elongation factor, TEFM, recently described by Minczuk and colleagues (12), on transcription of mtDNA. This protein was pulled down from mitochondrial lysates via mtRNAP and was found to stimulate nonspecific transcription on promoterless DNA; however, its effect on promoter-driven transcription had not been

determined (12). We found that in the presence of TEFM, mtRNAP efficiently transcribes through CSBII (Fig. 1, A and B). Thus, TEFM acts as a factor that prevents termination at CSBII and synthesis of a primer for mtDNA polymerase. We identified the exact location of the termination point in CSBII (fig. S1). MtRNAP terminates at the end of a U6 sequence (positions 287 to 283 in mtDNA), 16 to 18 nucleotides (nt) downstream of the G-quadruplex (Fig. 1A). At this point, the 9-bp RNA-DNA hybrid in the elongation complex (EC) is extremely weak, as it is composed of only A-U and T-A pairs. This is reminiscent of intrinsic termination signals in prokaryotes—where the formation of an RNA hairpin is thought to disrupt the upstream region of the RNA-DNA hybrid—and is followed by the run of six to eight uridine 5'-monophosphate residues that further destabilizes the complex (5, 13).

Human mtDNA is highly polymorphic in the CSBII region; coincidentally, the reference mitochondrial genome (Cambridge) contains a rare polymorphism in the G-quadruplex—namely, G5AG7—whereas the majority of mtDNAs from various haplogroups have two additional G residues (G6AG8) (14). We found that the termination efficiency of mtRNAP was substantially lower at G5AG7-CSBII (Fig. 1C), which suggested an effect of G run length on quadruplex formation and underscored the importance of further studies of various polymorphisms in this region.

In considering a putative mechanism of TEFM antitermination activity, we investigated whether it can interact with the nascent transcript and, thus, interfere with the formation of the quadruplex structure. We assembled ECs on a nucleic acid scaffold containing a photoreactive analog of uridine, 4-thio-uridine, 13 nt downstream from the 3' end of RNA, and walked mtRNAP along the template by incorporation of appropriate substrate nucleoside triphosphates (NTPs) (Fig. 2A). We observed efficient cross-linking between TEFM and RNA when the photoreactive base was 15 to 16 bp away from the 3' end of RNA. Additionally, using a template DNA containing the LSP promoter and

Department of Cell Biology, School of Osteopathic Medicine, Rowan University, 2 Medical Center Drive, Stratford, NJ 08084, USA.

*Corresponding author. E-mail: temiakdm@rowan.edu

Supplementary Material for Expansion Microscopy

Fei Chen, Paul W. Tillberg, Edward S. Boyden*

*Corresponding author. E-mail: esb@media.mit.edu

Published 15 January 2015 on *Science* Express
DOI: 10.1126/science.1260088

This PDF file includes:

Materials and Methods
Figures S1 to S5
Tables S1 to S4
Full Reference List

Other Supplementary Material for this manuscript includes the following:
(available at www.sciencemag.org/content/science.1260088/DC1)

Movies S1 to S3

Supplementary Materials:

Materials and Methods

A complete list of chemicals and supplier catalog numbers used can be found in **Table S2**.

Labels for ExM: DNA sequences on secondary antibodies were synthesized with 5' amine modification (Integrated DNA Technologies) and conjugated to the antibodies (Jackson ImmunoResearch, Affinipure donkey antibodies) using a commercial kit (Solulink, Antibody-Oligonucleotide All-in-One Conjugation Kit). For the tri-functional label, the oligonucleotides were synthesized with a 3' amine modification and a 5' Acrydite modification (Integrated DNA Technologies), then conjugated to dyes (Alexa 488, Atto 565 and Atto 647N) modified with NHS-ester chemistry per the dye manufacturer's directions (see **Table S3** for sequences). We found that Cy5 undergoes strong bleaching during polymerization, most likely due to the radical reactivity of its simple linear conjugated backbone, while other fluorophores tested retained at least 50% of their brightness (**Table S1**). Tri-functional labels were purified via reverse-phase HPLC, lyophilized, and re-suspended in ddH₂O.

Cultured cell preparation and staining: HEK293-FT cells (Invitrogen) were cultured in Culturewell Chambered Coverglasses (Invitrogen) per manufacturer's instructions. All solutions below were made up in 1x phosphate buffered saline (PBS), and incubations carried out at room temperature. To preserve microtubule ultrastructure, cells were fixed, as in (6), in 3% formaldehyde/0.1% glutaraldehyde for 10 minutes, followed by reduction with 0.1% NaBH₄ for 7 minutes, and quenching in 100 mM glycine for 10 minutes. For clathrin, cells were fixed in 4% formaldehyde for 10 minutes followed by quenching in 100 mM glycine for 10 minutes. Cells were permeabilized with 0.2% Triton X-100 for 15 minutes at room temperature and blocked with 5% normal donkey serum for one hour. Specimens were incubated with primary antibodies (Sheep anti-Tubulin, Cytoskeleton ATN02; Rabbit anti-Clathrin, Abcam AB21679) in blocking buffer at a concentration of 10 µg/mL for 1-4 hours, and then washed in PBS three times for 5 minutes each. Specimens were incubated with DNA-labeled secondary antibodies in DNA hybridization buffer (2x saline-sodium citrate (SSC) buffer, 10% dextran sulfate, 1 mg/mL yeast tRNA, 5% normal donkey serum) at a concentration of approximately 10 µg/mL for 1-4 hours, then washed in PBS as for primary. Specimens were incubated with tri-functional labels in hybridization buffer at a concentration of 0.5 ng/µL for each oligonucleotide overnight, then washed three times in 1x PBS.

Brain tissue preparation and staining: All procedures involving animals were in accordance with the US National Institutes of Health Guide for the Care and Use of Laboratory Animals and approved by the Massachusetts Institute of Technology Committee on Animal Care. All solutions below were made up in 1x phosphate buffered saline (PBS), and incubations carried out at room temperature unless otherwise noted. Mice, wildtype (C57BL/6, obtained from Taconic) and transgenic expressing cytosolic YFP under the Thy1 promoter (Thy1-YFP-H strain on C57BL/6, obtained from Jax), were anesthetized with isoflurane and perfused transcardially with ice cold 4% paraformaldehyde. Brains were dissected out, left in 4% paraformaldehyde at 4°C for one day, and then sunk in 30% sucrose with 100 mM glycine for one day. Slices greater than 30 µm thick were sliced on a vibratome (Leica VT1000S); slices 30 µm thick were frozen in -40°C isopentane cooled with dry ice, embedded in M-1 embedding matrix (Thermo Scientific) and sliced on a cryotome (Leica CM1850UV). Slices were permeabilized and blocked

with 0.1% Triton X-100 and 2% normal donkey serum (slice blocking buffer) for at least six hours. Slices were incubated with primary antibodies in slice blocking buffer at a concentration of 10 µg/mL for 6-24 hours depending on slice thickness and antibody, and then washed in slice blocking buffer four times, for thirty minutes each time, changing solutions in between. Slices were incubated with DNA-labeled secondary antibodies in hybridization buffer plus 0.1% Triton X-100 at a concentration of approximately 10 µg/mL for 6-24 hours depending on slice thickness and antibody, then washed in slice blocking buffer as for primary. Specimens were incubated with tri-functional labels in hybridization buffer plus 0.1% Triton X-100 at a concentration of 0.5 ng/µL per oligonucleotide for 6-12 hours, then washed in slice blocking buffer as for primary. Slices used were 30 µm (for the bleaching experiments of **Table S1**), 200 µm (**Fig. 1**, **Fig. S2**), or 100 µm (all other figures with slices) thick.

For **Figs. 3** and **4**, slices were stained with primary antibodies Chicken anti-GFP, Millipore AB16901; Rabbit anti-Homer1, Synaptic Systems 160003; Mouse anti-Bassoon, Abcam AB82958. For **Fig. S4**, antibodies used were Rabbit anti-GAD65/67, Chemicon AB1511; Rabbit anti-ChAT, Millipore AB143; Rabbit anti-CaMKII, Epitomics 2048-1; Rabbit anti-GABA, Sigma A2052; Mouse anti-Lamin A/C, Cell Signaling Technology #4777; Rabbit anti-NMDAR2a/b, Millipore AB1548.

In situ polymer synthesis: Monomer solution (1x PBS, 2 M NaCl, 8.625% (w/w) sodium acrylate, 2.5% (w/w) acrylamide, 0.15% (w/w) N,N'-methylenebisacrylamide) was mixed (see **Table S4**), frozen in aliquots, and thawed before use. Prior to embedding, monomer solution was cooled to 4°C to prevent premature gelation. Concentrated stocks (10% w/w) of ammonium persulfate (APS) initiator and tetramethylethylenediamine (TEMED) accelerator were added to the monomer solution up to 0.2% (w/w) each. For slices, the inhibitor 4-hydroxy-2,2,6,6-tetramethylpiperidin-1-oxyl (4-hydroxy-TEMPO) was added up to 0.01% (w/w) from a 1% (w/w) stock to inhibit gelation during diffusion of the monomer solution into tissue sections. Stained cells or tissue slices were incubated with the monomer solution plus APS/TEMED (and 4-hydroxy-TEMPO for slices) at 4°C for one minute, 30 minutes or 45 minutes for cultured cells, 30 µm/100 µm slices and 200 µm slices respectively. Slices were incubated with at least 100-fold excess volume of monomer solution.

For cells, gels were formed directly in a Culturewell Chambered Coverglass (Invitrogen), with monomer solution plus APS/TEMED added to a depth of about 2mm. For tissue slices, gelation chambers were constructed with two pieces of coverglass separated by spacers placed on either side of the tissue section (for 30 and 100 µm sections, #1 coverglasses were used for spacers and for 200 µm sections, a stack of two # 1 coverglasses was used for each spacer). Slices were not placed into coverglass gelation chambers until the end of the monomer incubation period, to ensure adequate access of the monomer solution to the slice. After incubation in monomer solution (and chamber construction, for slices), specimens were transferred to a humidified 37° C incubator for two hours.

Specimen-free gels of **Fig. S5** were cast with the same recipe as for cultured cells except with a variable amount of cross-linker, in forms constructed from two coverslips separated by a silicone gasket 1 mm thick, with circular holes 5.2 mm in diameter. Gels were expanded as with cultured cells, but without needing digestion. Diameters of expanded gels were measured using Vernier calipers to find the linear expansion factor.

Digestion and expansion: Proteinase K (New England Biolabs) was diluted 1:100 to 8 units/mL in digestion buffer (50 mM Tris (pH 8), 1 mM EDTA, 0.5% Triton X-100, 0.8 M guanidine HCl) and applied directly to gels in at least ten times volume excess. Before adding digestion buffer, the coverglass chamber walls (for cultured cells) or the top coverglass of the gelation chamber (for tissue slices) was carefully removed in order to improve access of enzyme to the embedded cells. The gels were then incubated in digestion buffer for at least 12 hours. Digested gels were next placed in excess volumes of doubly de-ionized water for 0.25-2 hours to expand, with longer times for thicker gels. This step was repeated 3-5 times in fresh water, until the size of the expanding sample plateaued.

Acrydite covalent anchoring efficiency: Label DNA oligonucleotides (A1 and A2, in **Table S3**) were ordered from IDT without the 5' acrydite modification, for the anchoring efficiency experiments of **Table S1**. Specimen-free gels ($n = 4$ gels) were cast with the same recipe as for cultured cells with addition of DNA labels with and without acrydite modification (0.25 ng/ μ L of each strand). Following gelation, gels were dialyzed in 20x volume of 10x PBS for 1 day to allow unincorporated DNA labels to equilibrate in concentration with the dialysate. Samples were taken from the dialysate after equilibration and measured on a fluorescence plate reader (Spectramax M5e). A fluorescence standard curve made from serial dilutions of label oligonucleotides was used to determine fluorescence concentration in the dialysate. The incorporation efficiency of non-acrydite labels was confirmed to be zero by fluorescence microscopy of the gels following dialysis equilibration; the ratio of fluorescence intensity inside the gel to the dialysate was 0.99 ± 0.07 ($n = 4$ samples). Acrydite incorporation efficiency was calculated as $1 - (\text{dialysate concentration with acrydite/dialysate concentration without acrydite})$.

Chemical bleaching during gelation: Fluorescence intensity in stained brain slices was measured before vs. after expansion for the bleaching experiments of **Table S1**. Wild type brain slices (30 μ m thick) containing sections of mouse hippocampus were stained with anti-GABA primary (Sigma A2052) antibody, DNA secondary antibodies, and tertiary DNA bearing either Alexa 488, Atto 565, or Atto 647N as described above. Epifluorescence images of the brain slice were taken with 4x 0.13 NA objective with tiling to cover the entire slice, pre-gelation. Following *in situ* polymer synthesis as described above, epifluorescence images of the slice were taken again with identical imaging conditions. A region of interest in the hippocampus was used to determine the loss of fluorescence during gelation.

Imaging:

Cultured cells. Super-resolution structured illumination microscope imaging was performed on a Deltavision OMX SIM microscope with 100x 1.40 NA (Olympus) oil objective. Stained cells were imaged with SlowFade Gold (Invitrogen) antifade reagent for suppression of photobleaching and refractive index matching for pre-expansion imaging. Pre-expansion imaging was performed on a Zeiss Laser Scanning Confocal (LSM710) with 40x 1.30 NA oil objective at 1 Airy unit and Nyquist sampling.

Post-expansion imaging was performed on a Perkin Elmer spinning disk (CSU-10 Yokogawa) confocal or a Zeiss LSM 710. Briefly, expanded samples were placed in glass-bottom six-well plates (In Vitro Scientific) and held in place by surrounding with low-melting point agarose. Images were taken at with 1 Airy unit and Nyquist sampling on the LSM 710 on a 20x 0.8 NA (Zeiss) air objective. Images on the Perkin Elmer were taken on a 100x 1.40 NA (Zeiss) oil objective.

Figs. 2A, 2B are maximum intensity projections (MIPs) of 1.5 μm thickness (in pre-ExM distance units). **Figs. 2D, 2E** are MIPs of 1 μm thickness. **Figs. 2K, 2L** are MIPs of 500 nm thickness. The SR-SIM image of **Fig. 2M** is depicted interpolated such that the pixel size is the same as that of the corresponding ExM image of **Fig. 2N**.

Brain slices. To quantify expansion factor for tissue slices, specimens were imaged pre-ExM on a Nikon Ti-E epifluorescence microscope with a 4x 0.13 NA air objective. Otherwise, tissue slices were imaged using an Andor spinning disk (CSU-X1 Yokogawa) confocal system with a 40x 1.15 NA water immersion objective (Nikon) or, for **Fig. S1** and **Fig. S4E**, the Zeiss LSM 710 with 40x 1.1 NA water objective. For pre-ExM confocal imaging, stained slices were treated with an anti-fade buffer (0.05% (w/w) p-phenyldiamine, 20 mM Tris (pH 8.5), 100 mM NaCl). Expanded slices were, for **Figs. 3** and **4**, sandwiched between coverslips of appropriate size (e.g., 45 x 60 mm), forming a chamber which was then backfilled with water and sealed with epoxy. Specimens encapsulated in this way were stable for at least a few days.

Figs. 3E, 3G are maximum intensity projections (MIPs) of 500nm thickness (in pre-ExM distance units), chosen to match the axial extent captured in **Figs. 3D, 3F**, respectively, as closely as possible. **Fig. 3H** is a single z-slice.

For large volume imaging of the mouse hippocampus (**Fig. 4**), the encapsulated expanded specimen was tiled with an array of 12 by 5 z-stacks with ~20% overlap at the boundaries (Nikon). The tiled stacks were downsampled by a factor of 8 for 3D rendering and reconstructed with the ImageJ stitching plugin (19). Imaging of these 60 confocal z-stacks, in three colors, with filter switching between each color (required for the low-crosstalk imaging using CMOS cameras in the spinning disk microscope), took ~27 hours.

Optical clearing measurements: Transmission measurements of tissue sections before and after expansion were performed using transmitted white light illumination on a Nikon Ti-E inverted microscope with pass-band filters (480/20, 520/20, 572/20, 610/38) to quantify wavelength dependence, as presented in **Fig S2**. Briefly, 200 μm thick tissue sections were imaged before expansion and after expansion with a 4x 0.13 NA objective with tiling to cover the entire area of the slice. Light transmission was calculated by measuring the transmission intensity of a circular region of interest centered on the tissue slice normalized by the average light transmission absent of the tissue slice.

Post-ExM Residual YFP fluorescence measurements: Unlabeled brain slices (100 μm) from Thy1-YFP-H mice were gelled, digested and expanded as described above, to result in the digestion penetration experiments of **Fig. S1**. Slices were digested with proteinase K for 16 hours. Following digestion, residual YFP fluorescence in cortical pyramidal cells was imaged on a confocal microscope (LSM 710, 40x 1.10 NA water) with pinhole opened to maximum extent (16 Airy units; 16 μm optical sectioning) to collect the dim residual YFP fluorescence. A collection of 25 Z stacks from 2 brain slices were taken across most of the expanded slice thickness (400 μm). To quantify the residual fluorescence at each Z position, the stacks were processed in a custom Matlab script. Briefly, for each image, salt and pepper noise was removed with a [5x5] median filter and the image was segmented into three regions with two thresholds generated via Otsu's method (20). The lowest segment of pixel intensities was the background, the middle segment consisted of most of the processes and cell bodies, and the highest segment consisted of a subset of nuclei in which much higher YFP concentrations were present (e.g., see **Fig. 3D** for an example of such a hyper-bright nucleus). The middle segment of pixel intensities

was chosen for the analysis. For each stack, the processed images were averaged for each Z position. The average intensity for each Z position was normalized by the overall average intensity across all Z positions and all stacks for a given brain slice. The normalized average intensity as a function of Z is plotted in **Fig. S1** along with the mean-normalized stack-to-stack standard deviation for each Z position.

Microscopy analysis.

Spinning disk confocal image processing. Standard flattfield correction was performed as needed due to uneven illumination background. Specifically, background was subtracted with a 200 pixel wide ‘rolling ball’ algorithm as implemented in ImageJ (i.e., **Fig. 2E, 2L, Fig. 4**).

Expansion degree calculation. The expansion degree was determined by choosing two landmarks that could be clearly identified in both pre- and post-expansion images, measuring the distance between these landmarks, and calculating the ratio of this measurement pre- vs. post-expansion. These manually chosen points were used to register the images to each other using a similarity transform (i.e., translation, rotation, and scaling) and the resulting registered images were inspected visually to confirm reasonable registration over the entire specimen.

Non-rigid registration for analysis of measurement errors. Pre- and post-ExM images were first histogram equalized (i.e., for the entire histogram of pixel intensities across each image; Matlab) to each other. Masks were generated to exclude regions with no features by applying a Gaussian blur with a standard deviation of 8 pixels and manually choosing an intensity threshold below which to exclude pixels that were part of the background. (Gaussian blur was used only to generate masks, not for subsequent image processing.) Non-rigid registration between the images was performed using a B-spline-based registration package in Matlab (21) using manually selected control points carrying a penalty weight of 1. Registration was performed in four stages with B-spline grids increasing in density from 64 pixels per grid point to 8 pixels per grid point. Analysis of measurement error was performed as schematized in **Fig. S3**.

Microtubule full width at half maximum (FWHM): Intensity profiles perpendicular to microtubule orientation was taken averaging over a line profile width of 10 pixels (~150 nm). Intensity profiles were fit to a Gaussian using the Matlab ‘fit’ function and the FWHM calculated from the Gaussian fit.

Quantification of clathrin coated pit (CCP) radii: As performed for **Fig. 2O**. Super-resolution structured illumination microscope (SR-SIM) and ExM images of CCPs were first aligned via similarity transform using 2 control points across the field of view. CCPs were identified by visual inspection of ExM z-stacks, and were selected with a rectangular region of interest (ROI, ~2x diameter of pit) so that there were no neighboring pits or background punctate staining within an ROI. For each pit selected in the analysis, its ROI was used to crop the ExM image and corresponding SR-SIM image. A maximum intensity projection of the ExM image corresponding to the same depth of field as the SR-SIM image was chosen to adjust for different optical sectioning thickness, corresponding to ~2 ExM planes (~60 nm/plane in pre-expansion units) for each SR-SIM z-plane (125 nm/plane) chosen. CCP radii were calculated with angular averaging of a radial line profile originating from the centroid of each CCP, with the centroid calculated from the Otsu-binarized image. The angular radial line profile was fit using the Matlab ‘fit’ function to the sum of 2 Gaussians. The CCP radius was determined to be the half maximum of the fitted angular line profile.

Synapse quantification: Synapses of **Fig. 3** were identified by visual inspection of ExM z-stacks. Candidate instances of closely apposed Bassoon and Homer1 antibody-stained spots were selected from a maximum intensity projection of each stack. Each candidate was then inspected in the original z-stack and selected for inclusion in the analysis if it did not meet any of the following rejection criteria: synapses that were not oriented perpendicular to the imaging plane were recognized when the stained spots shifted continuously between consecutive z-slices, and were rejected; synapses with coincident punctate background staining were rejected; complex assemblies of synapses (e.g., with multiple pre- or post-synaptic terminals) were rejected; synapses that were excessively curved (e.g., relative to the 10-pixel line width, see below) were rejected. For each synapse selected for inclusion in the analysis, a line profile perpendicular to the synaptic cleft was chosen. The staining intensity for Bassoon and Homer1 was analyzed along each line profile, averaging over a width of 10 pixels (~ 300 nm). The resulting intensity distributions were fit to Gaussian distributions with a DC offset using the Matlab ‘fit’ function. Any synapses with a resulting goodness of fit, for either Homer1 or Bassoon, of less than 0.9 were rejected. The Bassoon-Homer1 separation was calculated as the separation between the means of the two distributions for each synapse.

Supplementary Figures

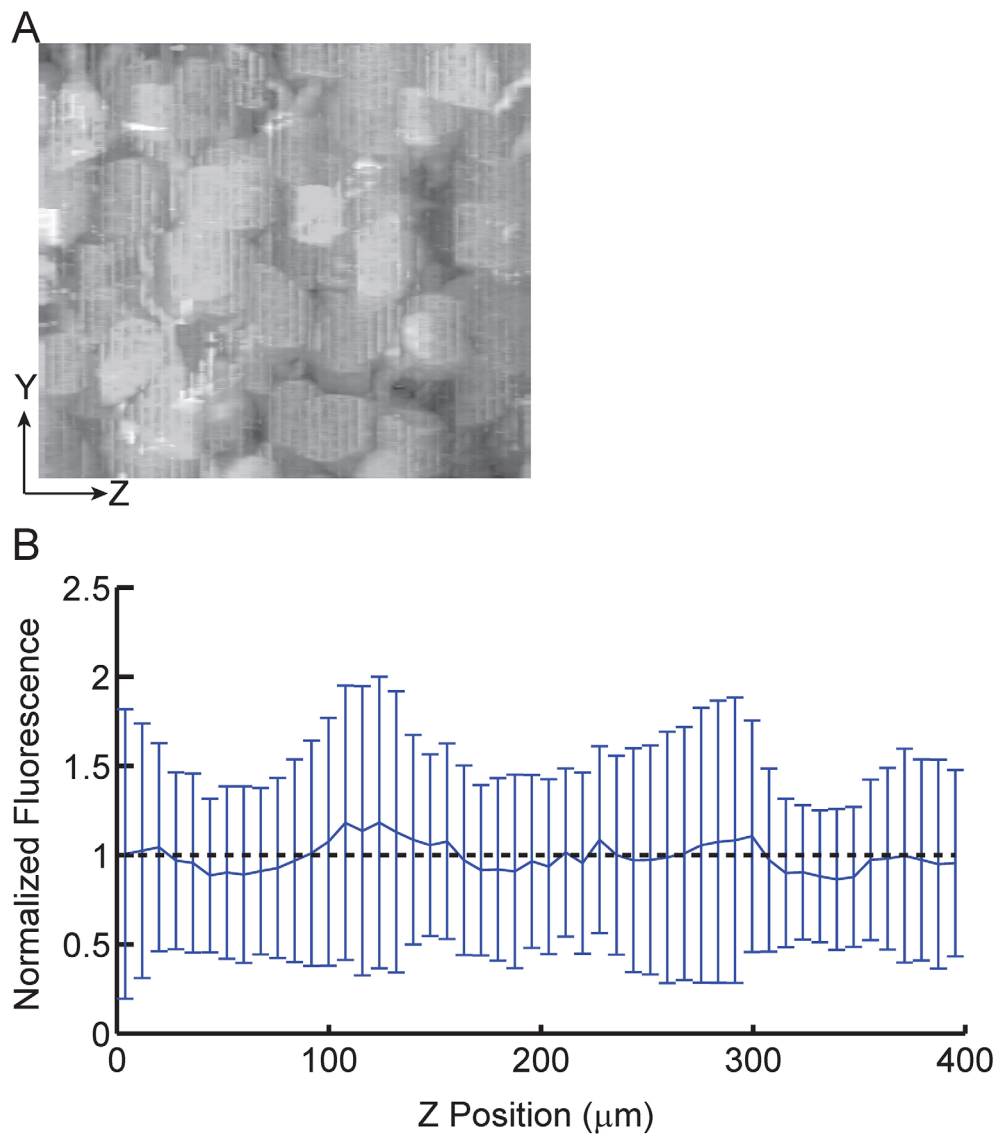


Figure S1. Residual YFP fluorescence as a function of depth in the slice, after digestion and expansion. Proteolysis during the ExM process significantly reduces endogenous YFP fluorescence in expanded samples of Thy1-YFP mouse brain. The residual YFP fluorescence can thus be imaged as a proxy for proteolytic homogeneity. **(A)** Maximum intensity projection in the X dimension of 25 Z stacks of pyramidal cells in the cortex of Thy1-YFP-H brain slices after overnight digestion and subsequent expansion, and processed to exclude high-brightness nuclei and background as described in the **Methods**. The length in the Z dimension is 400 μm in post-expanded units (almost all of the thickness of the 100 μm slice after $\sim 4.5\times$ expansion). **(B)** Mean fluorescence intensity across the stacks of **(A)**, normalized by overall mean fluorescence, plotted as a function of Z. Error bars, mean-normalized stack-to-stack standard deviation ($n = 25$ Z stacks, 2 brain slices). Dotted line, visual reference for fluorescence equal to the mean. The lack of systematic variation of YFP fluorescence vs. depth demonstrates the uniformity of proteolytic digestion throughout the slice.

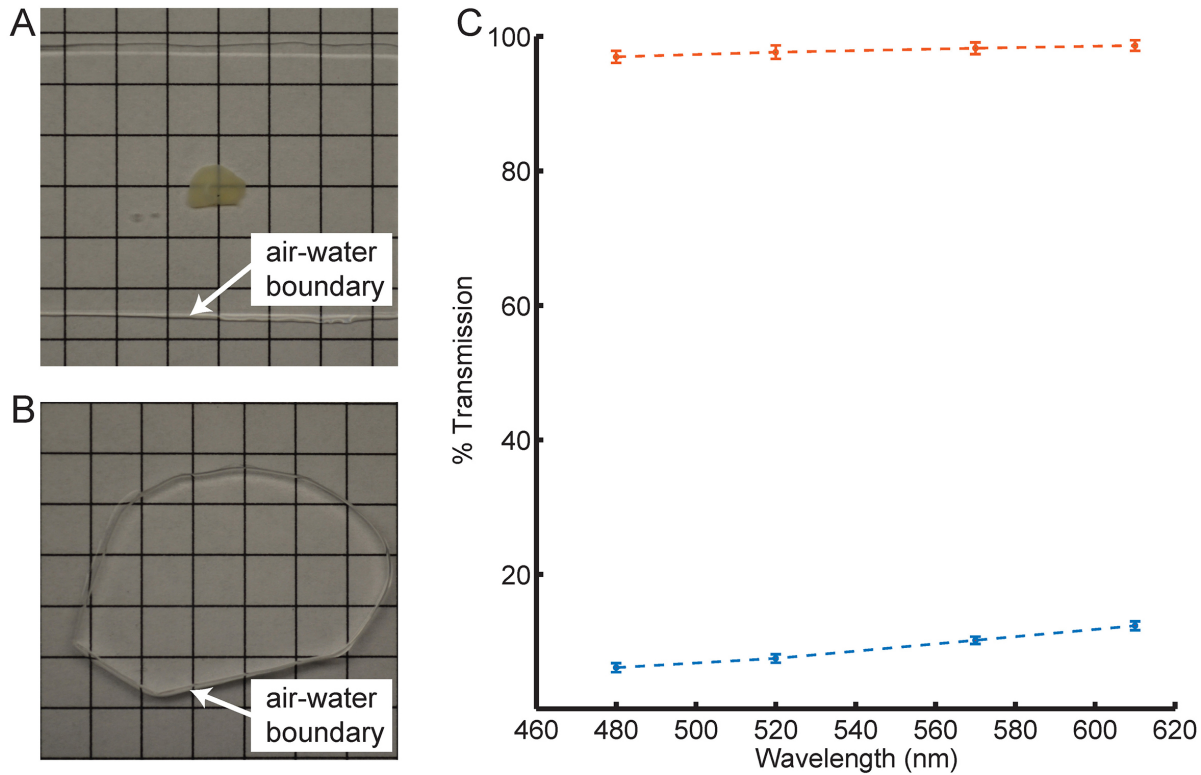


Figure S2. Optical clearing associated with ExM. Expansion significantly reduces scattering of the sample, since the sample is mostly water. A 200 μm fixed brain slice is opaque primarily due to scattering (**A**). However, the post-ExM sample is transparent (**B**). We quantified the transmittance of light through the tissue pre- (blue) vs. post- (orange) ExM processing (**C**).

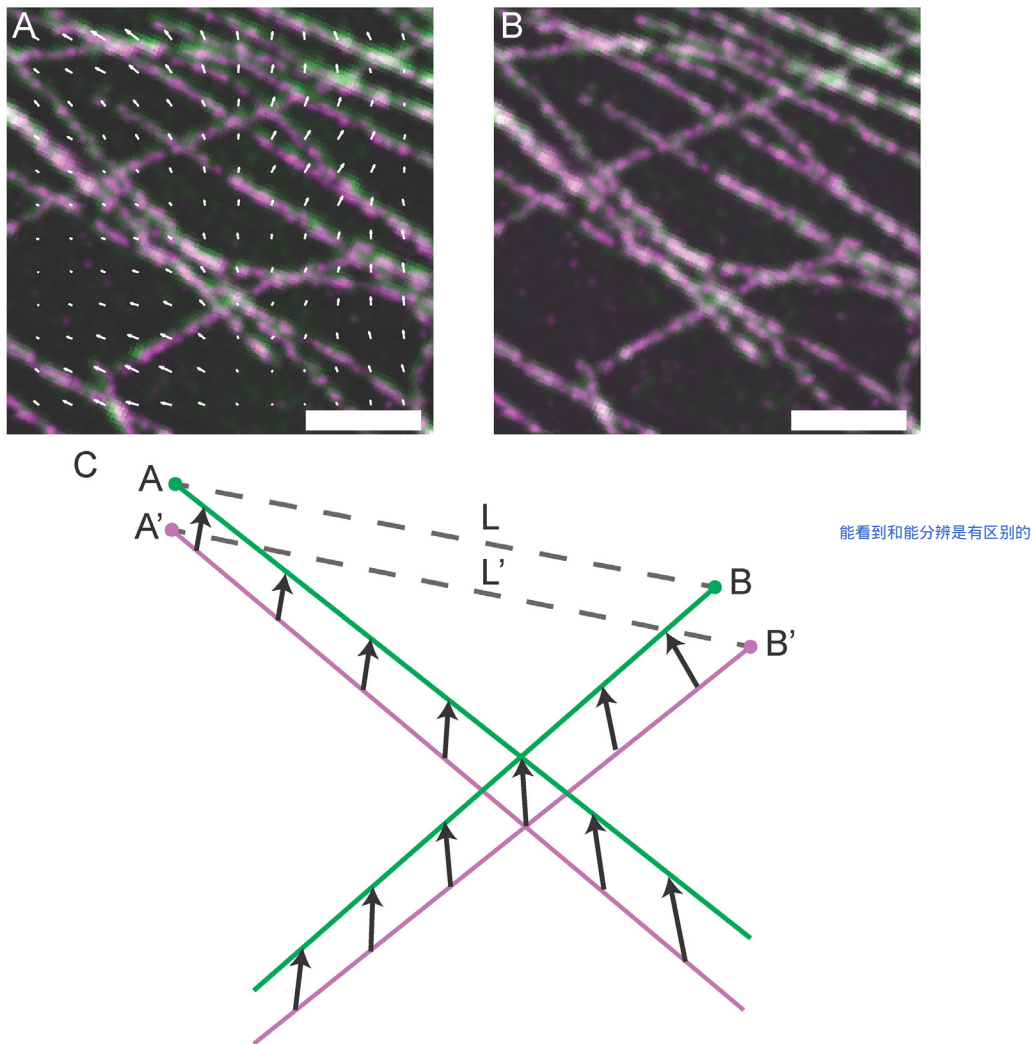


Figure S3. Quantification of Expansion Error Using Non-Rigid Registration. We quantified the error of ExM by deforming the post-ExM image via a non-rigid registration process to attempt an exact match to the pre-ExM image (in contrast to the similarity transform used in Fig. 2A, 2B and elsewhere). We used a B-spline based non-rigid registration algorithm (see Methods) which generates a vector field that maps the post-ExM image (**A**, magenta) to the pre-ExM image (**B**, green). In (**A**) the overlap between the pre- and post-ExM images appears white, and the deformation vector field (white arrows) is plotted with vector magnitudes scaled by factor of 2 for visibility. The post-ExM image after deformation (**B**, magenta) colocalizes with the pre-ExM image (**B**, green; overlap appears white). Using this deformation field, we can calculate the error of ExM for various length measurements. This is schematized in (**C**): the magenta lines, representing structures in the post-ExM image, are mapped to the green lines, representing the pre-ExM image, via the vector field depicted by black arrows. Measurement L' along the line segment $A'B'$ in the post-ExM image is mapped to measurement L along the line segment AB in the pre-ExM image. The ExM error is calculated as $|L-L'|$, i.e. the difference between the deformation vectors AA' and BB' . Using the deformation field generated we can calculate the ExM error between all extracted features in the pre- vs. post- images. Scale bars: 1 μm .

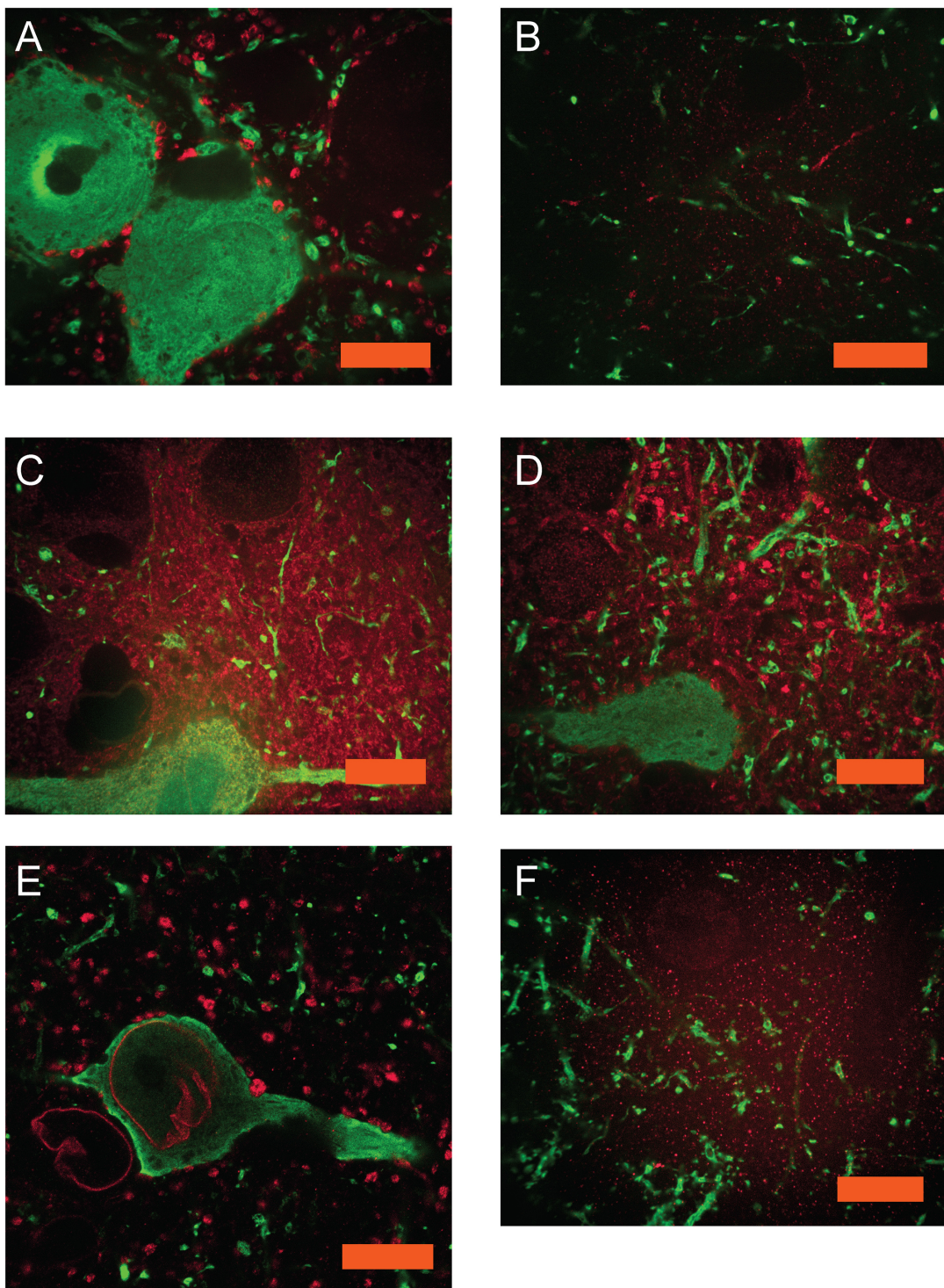


Figure S4. ExM imaging of antibodies of interest in neuroscience and biology. Confocal images of expanded Thy1-YFP mouse brain cerebral cortex sections stained with anti-GFP (green) and antibodies against other proteins (red) as follows: **(A)** GAD65/67 (22), **(B)** ChAT (23), **(C)** CaMKII (24), **(D)** GABA (25), **(E)** Lamin A/C (26), **(F)** NMDAR2a/b (27). Scale bars: **(A)** 10 μ m in pre-expansion units (physical size post-expansion, 45 μ m); **(B)** 10 μ m (47 μ m); **(C)** 10 μ m (40 μ m); **(D)** 10 μ m (44 μ m); **(E)** 10 μ m (43 μ m); **(F)** 10 μ m (43 μ m).

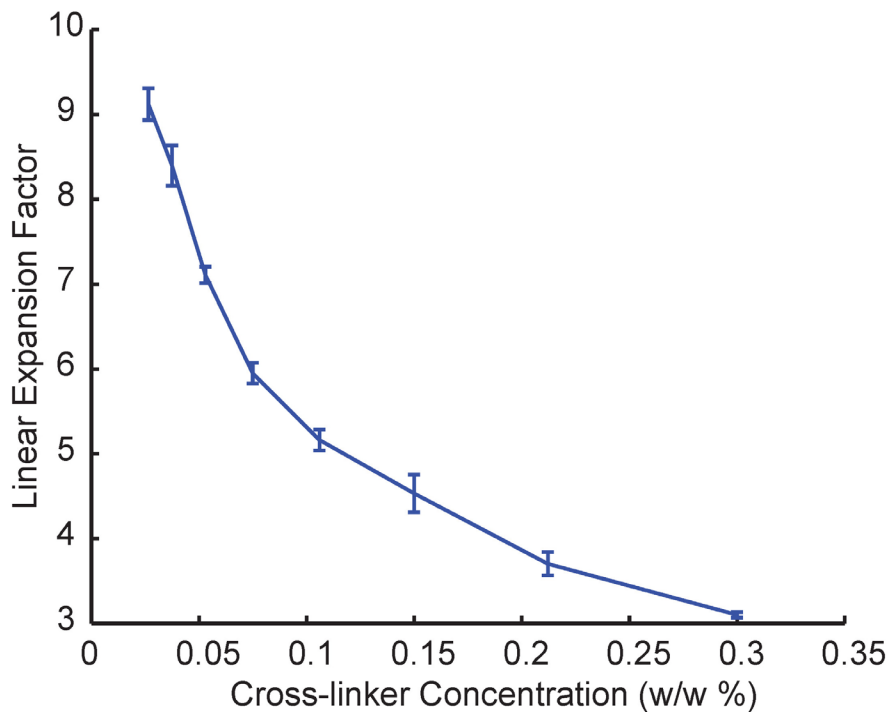


Figure S5. Expansion factor vs. cross-linking. Linear expansion factor for gels cast without specimens, as a function of the concentration of cross-linker used. Error bars represent standard deviation ($n = 4$ samples).

Supplementary Tables

Table S1. Fluorescence retention during ExM chemical steps.

Fluorescence Retention After Gelation		
	Percent Retention	Standard Deviation (%)
Alexa 488	57.2	2.9 ($n = 2$ slices)
Atto 565	76.2	0.5 ($n = 2$ slices)
Atto 647N	58.5	2.8 ($n = 2$ slices)
Covalent Anchoring Efficiency During Gelation		
	Percentage Anchored	Standard Deviation (%)
Acrydite DNA	87.2	1.1 ($n = 4$ gels)

Table S2. Chemicals list and suppliers.

	Chemical Name	Supplier	Part Number
ExM Gel or Preparation	Sodium Acrylate	Sigma	408220
	Acrylamide	Sigma	A9099
	N,N'-Methylenebisacrylamide	Sigma	M7279
	Ammonium Persulfate	Sigma	A3678

	N,N,N',N'-Tetramethylethylenediamine	Sigma	T7024
	4-Hydroxy-TEMPO	Sigma	176141
Fluorescent Dyes	Alexa 488 NHS ester	Life Technologies	A-20000
	Atto 565 NHS Ester	Sigma	72464
	Atto 647N NHS Ester	Sigma	18373
Hybridization Buffer	Dextran Sulfate	Millipore	S4030
	SSC	Life Tech.	15557
	Yeast tRNA	Roche	10109495001
	Normal Donkey Serum	Jackson Immunoresearch	017-000-001
Fixation and Permeabilization	Paraformaldehyde	Electron Microscopy Sciences	15710
	Glutaraldehyde	Electron Microscopy Sciences	16020
	Triton X-100	Sigma	93426
	Glycine	Sigma	50046
	PBS	Life Technologies	70011-044
Protein Digestion	Proteinase K	New England Biolabs	P8107S
	Ethylenediaminetetraacetic acid	Sigma	EDS
	Guanidine HCl	Sigma	G3272
	Tris-HCl	Life Technologies	AM9855

Table S3. DNA sequences and modifications used for tri-functional labels.

All DNA sequences were ordered from Integrated DNA Technologies, and adapted from (28). Each strand for antibody conjugation consists of two 20bp domains separated by two bases of A/T.

Name	Sequence	Modifications
Antibody A	CCGAATAACAAAGCATCAACG AA GGTGACAGGGATCACAAATCT	5' Amine
Antibody B	TACGCCCTAAGAACATCCGAAC TT GCATTACAGTCCTCATAAGT	5' Amine
Antibody C	GACCCTAACGCATACATCGTC TT GACTACTGATAACTGGATTG	5' Amine

Two complementary tri-functional label domains hybridize to each strand conjugated to an antibody. Each antibody strand corresponds to one color of dye.

Name	Sequence	Modifications
A1	CGTTGATGCTTGATTCTGG	5' Acrydite 3' A488
A2	AGATTGTGATCCCTGTCACC	5' Acrydite 3' A488
B1	GTTCGGATTCTTAGGGCGTA T	5' Acrydite 3' Atto 565
B2	ACTTATGAGGACTGTAATGC T	5' Acrydite 3' Atto 565
C1	GACGATGTATGCTTAGGGTC T	5' Acrydite 3' Atto 647N
C2	CAATCCAGTTATCAGTAGTC T	5' Acrydite 3' Atto 647N

Table S4. Monomer solution recipe.

Component	Stock concentration*	Amount (mL)	Final concentration*
Sodium acrylate	38	2.25	8.6
Acrylamide	50	0.5	2.5
N,N'-Methylenebisacrylamide	2	0.75	0.15
Sodium chloride	29.2	4	11.7
PBS	10x	1	1x
Water		1	
Total		9.5**	

*All concentrations in g/100 mL except PBS

This solution is stored as 0.95 mL aliquots, with initiator, accelerator and inhibitor (as needed; see **Methods) added to bring the final volume up to 1 mL per aliquot immediately before each experiment.

Supplementary Movies

Movie S1: 3D animation of large-scale rendering of hippocampal volume from **Fig. 4A**. First, the volume appears with YFP only (green), then staining for Bassoon (blue) and Homer1 (red) are added. Scale bars: 100 μ m.

Movie S2: 3D animation of rendered CA1 slm dendrites from **Fig 4B**. Scale bars: 10 μm .

Movie S3: 3D animation of rendered dendritic branch of CA1 slm from **Fig. 4C**, showing YFP (green), Bassoon (blue), and Homer1 (red). Scale bars: 2.5 μm .

Supplementary References

References 19-28 are for the supplementary materials.

References and Notes

1. T. Tanaka, D. Fillmore, S.-T. Sun, I. Nishio, G. Swislow, A. Shah, Phase transitions in ionic gels. *Phys. Rev. Lett.* **45**, 1636–1639 (1980). [doi:10.1103/PhysRevLett.45.1636](https://doi.org/10.1103/PhysRevLett.45.1636)
2. I. Ohmine, Salt effects on the phase transition of ionic gels. *J. Chem. Phys.* **77**, 5725 (1982). [doi:10.1063/1.443780](https://doi.org/10.1063/1.443780)
3. F. L. Buchholz, *Superabsorbent Polymers* **573**, 27–38 (1994).
4. B. Huang, S. A. Jones, B. Brandenburg, X. Zhuang, Whole-cell 3D STORM reveals interactions between cellular structures with nanometer-scale resolution. *Nat. Methods* **5**, 1047–1052 (2008). [Medline](#) [doi:10.1038/nmeth.1274](https://doi.org/10.1038/nmeth.1274)
5. E. H. Rego, L. Shao, J. J. Macklin, L. Winoto, G. A. Johansson, N. Kamps-Hughes, M. W. Davidson, M. G. Gustafsson, Nonlinear structured-illumination microscopy with a photoswitchable protein reveals cellular structures at 50-nm resolution. *Proc. Natl. Acad. Sci. U.S.A.* **109**, E135–E143 (2012). [Medline](#) [doi:10.1073/pnas.1107547109](https://doi.org/10.1073/pnas.1107547109)
6. M. Bates, B. Huang, G. T. Dempsey, X. Zhuang, Multicolor super-resolution imaging with photo-switchable fluorescent probes. *Science* **317**, 1749–1753 (2007). [Medline](#) [doi:10.1126/science.1146598](https://doi.org/10.1126/science.1146598)
7. N. Olivier, D. Keller, P. Gönczy, S. Manley, *PLOS One* **8**, (2013). 10.1371/journal.pone.0069004
8. R. W. Cole, T. Jinadasa, C. M. Brown, Measuring and interpreting point spread functions to determine confocal microscope resolution and ensure quality control. *Nat. Protoc.* **6**, 1929–1941 (2011). [Medline](#) [doi:10.1038/nprot.2011.407](https://doi.org/10.1038/nprot.2011.407)
9. G. Feng, R. H. Mellor, M. Bernstein, C. Keller-Peck, Q. T. Nguyen, M. Wallace, J. M. Nerbonne, J. W. Lichtman, J. R. Sanes, Imaging neuronal subsets in transgenic mice expressing multiple spectral variants of GFP. *Neuron* **28**, 41–51 (2000). [Medline](#) [doi:10.1016/S0896-6273\(00\)00084-2](https://doi.org/10.1016/S0896-6273(00)00084-2)
10. A. Dani, B. Huang, J. Bergan, C. Dulac, X. Zhuang, Superresolution imaging of chemical synapses in the brain. *Neuron* **68**, 843–856 (2010). [Medline](#) [doi:10.1016/j.neuron.2010.11.021](https://doi.org/10.1016/j.neuron.2010.11.021)
11. A. Rollenhagen, J. H. R. Lübke, The mossy fiber bouton: The “common” or the “unique” synapse? *Front. Synaptic Neurosci.* **2**, 2 (2010). [Medline](#)
12. G. R. Newman, B. Jasani, E. D. Williams, A simple post-embedding system for the rapid demonstration of tissue antigens under the electron microscope. *Histochem. J.* **15**, 543–555 (1983). [Medline](#) [doi:10.1007/BF01954145](https://doi.org/10.1007/BF01954145)
13. K. D. Micheva, S. J. Smith, Array tomography: A new tool for imaging the molecular architecture and ultrastructure of neural circuits. *Neuron* **55**, 25–36 (2007). [Medline](#) [doi:10.1016/j.neuron.2007.06.014](https://doi.org/10.1016/j.neuron.2007.06.014)
14. B.-C. Chen, W. R. Legant, K. Wang, L. Shao, D. E. Milkie, M. W. Davidson, C. Janetopoulos, X. S. Wu, J. A. Hammer 3rd, Z. Liu, B. P. English, Y. Mimori-Kiyosue, D. P. Romero, A. T. Ritter, J. Lippincott-Schwartz, L. Fritz-Laylin, R. D. Mullins, D. M. Mitchell, J. N. Bembek, A. C. Reymann, R. Böhme, S. W. Grill, J. T. Wang, G.

Seydoux, U. S. Tulu, D. P. Kiehart, E. Betzig, Lattice light-sheet microscopy: Imaging molecules to embryos at high spatiotemporal resolution. *Science* **346**, 1257998 (2014). [Medline doi:10.1126/science.1257998](#)

15. J. Huisken, J. Swoger, F. Del Bene, J. Wittbrodt, E. H. K. Stelzer, Optical sectioning deep inside live embryos by selective plane illumination microscopy. *Science* **305**, 1007–1009 (2004). [Medline doi:10.1126/science.1100035](#)
16. J. H. Lee, E. R. Daugherty, J. Scheiman, R. Kalhor, J. L. Yang, T. C. Ferrante, R. Terry, S. S. Jeanty, C. Li, R. Amamoto, D. T. Peters, B. M. Turczyk, A. H. Marblestone, S. A. Inverso, A. Bernard, P. Mali, X. Rios, J. Aach, G. M. Church, Highly multiplexed subcellular RNA sequencing *in situ*. *Science* **343**, 1360–1363 (2014). [Medline doi:10.1126/science.1250212](#)
17. A. M. Hecht, R. Duplessix, E. Geissler, Structural inhomogeneities in the range 2.5–2500. ANG. in polyacrylamide gels. *Macromolecules* **18**, 2167–2173 (1985). [doi:10.1021/ma00153a018](#)
18. D. Calvet, J. Y. Wong, S. Giasson, Rheological monitoring of polyacrylamide gelation: Importance of cross-link density and temperature. *Macromolecules* **37**, 7762–7771 (2004). [doi:10.1021/ma049072r](#)
19. S. Preibisch, S. Saalfeld, P. Tomancak, Globally optimal stitching of tiled 3D microscopic image acquisitions. *Bioinformatics* **25**, 1463–1465 (2009). [Medline doi:10.1093/bioinformatics/btp184](#)
20. N. Otsu, A threshold selection method from gray-level histograms. *IEEE Trans. Syst. Man Cybern.* **9**, 62–66 (1979). [doi:10.1109/TSMC.1979.4310076](#)
21. D.-J. Kroon, “B-spline Grid, Image and Point based Registration”; available at www.mathworks.com/matlabcentral/fileexchange/20057-b-spline-grid--image-and-point-based-registration.
22. C. E. Ribak, Aspinous and sparsely-spinous stellate neurons in the visual cortex of rats contain glutamic acid decarboxylase. *J. Neurocytol.* **7**, 461–478 (1978). [Medline doi:10.1007/BF01173991](#)
23. C. R. Houser, G. D. Crawford, P. M. Salvaterra, J. E. Vaughn, Immunocytochemical localization of choline acetyltransferase in rat cerebral cortex: A study of cholinergic neurons and synapses. *J. Comp. Neurol.* **234**, 17–34 (1985). [Medline doi:10.1002/cne.902340103](#)
24. B. Tighilet, T. Hashikawa, E. G. Jones, Cell- and lamina-specific expression and activity-dependent regulation of type II calcium/calmodulin-dependent protein kinase isoforms in monkey visual cortex. *J. Neurosci.* **18**, 2129–2146 (1998). [Medline](#)
25. S. H. C. Hendry, E. G. Jones, P. C. Emson, D. E. Lawson, C. W. Heizmann, P. Streit, Two classes of cortical GABA neurons defined by differential calcium binding protein immunoreactivities. *Exp. Brain Res.* **76**, 467–472 (1989). [Medline doi:10.1007/BF00247904](#)
26. P. Hozák, A. M. Saserville, Y. Raymond, P. R. Cook, *J. Cell Sci.* **108**, 635–644 (1995).

27. J. M. Fritschy, O. Weinmann, A. Wenzel, D. Benke, Synapse-specific localization of NMDA and GABA_A receptor subunits revealed by antigen-retrieval immunohistochemistry. *J. Comp. Neurol.* **390**, 194–210 (1998). [Medline doi:10.1002/\(SICI\)1096-9861\(19980112\)390:2<194::AID-CNE3>3.0.CO;2-X](#)
28. H. M. T. Choi, J. Y. Chang, A. Trinh, J. E. Padilla, S. E. Fraser, N. A. Pierce, Programmable in situ amplification for multiplexed imaging of mRNA expression. *Nat. Biotechnol.* **28**, 1208–1212 (2010). [Medline doi:10.1038/nbt.1692](#)